Iron Pyrite Nanocubes: Size and Shape Considerations for Photovoltaic Application

H. Alex Macpherson and Conrad R. Stoldt*

Department of Mechanical Engineering, University of Colorado, Boulder, Colorado, United States

ABSTRACT

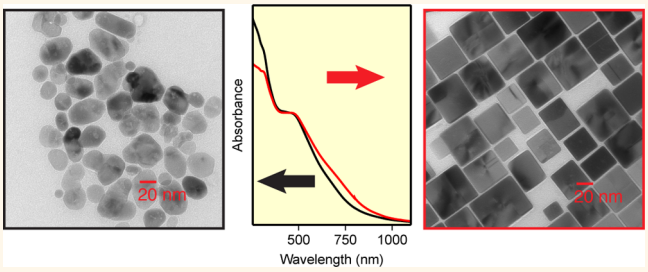

Multiple lines of recent research indicate that iron pyrite (FeS_2) requires a {100}-terminated crystal morphology in order to maintain semiconducting properties. Additionally, the large absorption coefficient of pyrite allows for the near complete absorption of above band gap radiation in <50 nm layers. However, to our knowledge <50 nm pyrite nanocubes have yet to be isolated. Herein, we demonstrate the synthesis of ~37 nm phase pure pyrite nanocubes by manipulating the sulfur chemical potential and ligand environment of the system. Ultraviolet–visible (UV–vis) absorption spectroscopy gives a signal of resonant light scattering indicating strong electronic coupling between nanocubes, which may allow for nanocube films with superior electron mobility. The absorption spectroscopies of cubic and irregular nanocrystals are contrasted and compared with recent theoretical work in order to investigate the effect of shape on electronic properties. Specifically, nanocubes have been found to have absorption characteristics closer to theory as compared to irregular nanocrystals, especially for UV radiation: 250–350 nm. Pyrite nanocubes display an indirect band gap at ~1.1 eV in addition to two direct transitions at ~1.9 and ~3.0 eV, correlating well to theoretical values.

KEYWORDS: nanocrystal · pyrite · photovoltaic · shape control · resonant light scattering

Iron pyrite (FeS_2, hereafter termed pyrite for simplicity) is a technologically important indirect band gap semiconductor ($E_g \approx 0.95$ eV). It has been commercialized as a high-capacity electrode material in lithium-ion primary batteries,[1] and recent developments indicate its viability in rechargeable batteries as well.[2] Understanding the surface chemistry of pyrite is an especially important issue for multiple applications. Recent work has identified the surface of pyrite as interesting for dilute magnetic semiconductor research with spintronic application.[3] Oxidative decomposition at pyrite's surface has become vital in understanding the processes leading to the acidification of runoff coming from coal mining, a phenomenon known as acid mine drainage.[4] However, the most active pyrite research effort is directed toward its potential application as the photoactive material in thin-film solar cells, an additional application that, as described below, necessitates a better understanding of its surface properties.

Concerning photovoltaics, pyrite's unique properties include an exceptionally large optical absorption coefficient in the visible region ($\alpha > 10^5$ cm^{-1} at $\hbar\omega > 1.5$ eV)[5] coupled with large elemental abundances, nontoxicity, and low material refinement costs.[6] Its single junction thermodynamic limit (Shockley–Queisser limit) is ~31%, slightly less than the 33.7% limit for an ideal band gap of 1.34 eV.[6] Therefore pyrite as the active material in photovoltaic junctions is well positioned to directly address the predominant challenge in solar harvesting, the economic difficulty of widespread deployment.

Furthermore, such high optical absorption in pyrite allows for absorption of 90% of incident light in only ~40 nm thick layers (neglecting light scattering).[7] If such ultrathin films can be formed, it could potentially enable more efficient carrier extraction and the creation of novel heterojunction device architectures such as extremely thin absorber cells, which can be considered "semiconductor-sensitized" in analogy to dye-sensitized cells.[8]

In the 1980s, work was undertaken to develop the technology, predominately by the Tributsch group in Germany, who succeeded in creating electrochemical cells with mostly favorable characteristics. However, the photovoltage remained around 200 mV in these cells, far below theoretical estimates and thereby limiting efficiencies to below

* Address correspondence to Conrad.Stoldt@Colorado.edu.

Received for review July 2, 2012 and accepted September 16, 2012.

Published online September 17, 2012
10.1021/nn3029502

3%.[7] This anomalously low open-circuit voltage has remained a persistent problem. With renewed interest, prompted mostly by the materials availability study of Wadia *et al.*,[6] theoretical studies have begun to bring the source of the problem into clearer focus.

Historically, the most common explanation for the anomalously low open-circuit voltage has been sulfur deficiencies in the bulk material.[9] However, recent theoretical work[10−12] and a survey of experimental studies[13] now suggest that pyrite is essentially a stoichiometric compound ($O(10^6)/cm^3$) with a sizable (~2.4 eV) sulfur defect formation energy. These same considerations have been used to argue against the presence of Fermi level pinning in the material.[10]

Another possible explanation for the low open-circuit voltage is that trace impurities of the orthorhombic polymorph (marcasite) or iron monosulfide (FeS) phases may exist and limit voltage. Concerning marcasite, recent modeling has shown that it may itself be a semiconductor and that while one or two layers may grow on pyrite surfaces, no midgap states are created.[14]

Considering surface structure, pyrite is commonly cleaved on either the {100}, {111}, or {210} face.[15] Work by Alfonso argues that both of the low-energy {111} and {210} faces create conductive surfaces.[16] The stoichiometric {100}-S faces (hereafter termed the {100} faces for simplicity), however, leave the surface basically unreconstructed and do not break bonds in the persulfide unit.[17] Therefore, surface iron atoms no longer have a distorted octahedral crystal field but are reduced to square-pyramidal symmetry. The band gap of pyrite at the (100) surface has been evaluated theoretically, with most studies showing only a slight decrease (0−0.3 eV) from the bulk value.[10,14,18,19]

As argued above, bulk considerations and the electronic state of the perfect {100} face have not been able to explain the observed low photovoltage. However photoelectron spectroscopy,[17] scanning tunneling microscopy,[20] and modeling[19] have firmly established that there is a low-energy route to defect states on the (100) surface. At the level of single sulfur defects Yu *et al.*[10] and Zhang *et al.*[18] both find that sulfur vacancies have low formation energies (~0.4 eV) on these faces, but differ regarding the relative impact on electronic properties. As the concentration of defect sites increases, there can be a large percentage of iron monosulfide defects with a surface charge rearrangement that oxidizes iron to Fe^{3+} and reduces sulfur to S^{2-}.[21] Effectively, an iron monosulfide shell may be created, and such defects could cause the observed conductive behavior indicated by low open-circuit voltage measurements.

With such a high optical absorption coefficient in pyrite (penetration depth: δ = ~15 nm in the visible)[5] most excitons are created in the near surface of the material, magnifying the importance of surface considerations. Therefore, it is probably unsurprising that the best device results with pyrite have come from surface treatments prior to the creation of electrochemical interfaces. Specifically the Tributsch group found that $HF/CH_3COOH/HNO_3$[22] and KCl[23] treatments markedly improved the electrochemical performance of their photoelectrodes. In addition many high-vacuum studies have found it necessary to wash their samples in acid prior to analysis to obtain a high-quality surface.[24]

Given the size constraint, recent studies have created pyrite by nanocrystal synthetic routes.[25−28] However, these studies either have not isolated {100} faces or have done so at sizes 150 nm or larger.[28] Photovoltaic devices with this particle size (>150 nm) will have a mismatch between penetration depth and device thickness, necessitating longer diffusion lengths and negating the inherent strengths of pyrite as an absorbing material.

Additionally, UV−vis absorption spectroscopy in these studies, while generally indicating an indirect transition around 1 eV, has been significantly different so as to obscure a consistent determination of the electronic properties of the material. Such ambiguity in characterization of the optical band gap seems to preclude the possibility that the electronic band gap, including interfaces, will be appropriate for optoelectronic applications.

In the work described here, we have attempted to address pyrite's synthetic challenges by nanocrystal synthesis in order to grow <50 nm particles with {100} faces. We use alkylamines of different lengths to constrain size and leverage theoretical data indicating that {100} faces are favored when the chemical potential of sulfur is low to manipulate shape.[16] The resulting cubic product reported here is amenable to various surface treatments that may help elucidate the surface processes active on the {100} facets; such work will be vital for photovoltaic application as well as surface magnetism and oxidative decomposition studies, as described above.

It should be noted that this type of study is somewhat unique in the field of semiconductor nanocrystals in that no attempt at quantum confinement is made. This has distinctly altered the common requirements for a successful synthesis. Monodispersity and size requirements (normally for emission purity) are considerably relaxed, whereas, as described above, shape and surface constraints are of primary importance.

RESULTS AND DISCUSSION

Synthetic Scheme. The general synthetic scheme described in this work uses the chemical potential of sulfur along with alkylamines of different lengths and temperature to control the size and shape of the product. Specifically, Figure 1 shows the transition from irregular particles after the nucleation step to

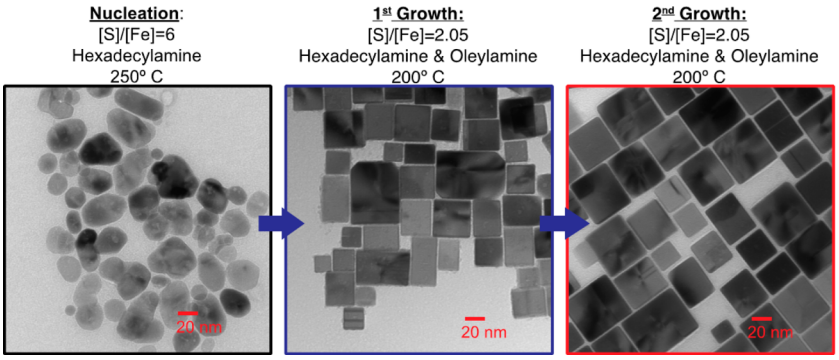

Figure 1. TEM images and chemical conditions indicating the synthetic scheme employed.

euhedral nanocubes after one growth step and further toward shape perfection after the second growth step. This figure also gives the solvent environments, molar sulfur/iron ratios, and temperatures employed to induce the indicated results. Here, and throughout this study, we use the term nucleation to mean the initial product of our synthesis rather than molecular seed crystals.

Figure 2A,B give additional TEM and HRTEM images of the final product of this synthesis, indicating the cubic morphology of the particles and the size distribution. Five-hundred nanocubes were measured from TEM images to give the size distribution histogram displayed in Figure 2C. The final product is measured to have an average edge length of 37 nm with a standard deviation of 11 nm. The measured lattice parameters estimated from HRTEM correspond well to accepted values.[29]

Structural and Elemental Characterization. Structural characterization of the resulting pyrite nanocubes is given in Figure 3. X-ray powder diffraction peaks in Figure 3A correlate well to pyrite with accepted lattice parameters (a = 5.418 Å, u = 0.385 Å).[29] No peaks corresponding to marcasite (FeS_2) or pyrrhotite (FeS) are detected, indicating phase purity for each growth step in the synthesis.

A Scherrer analysis of the final XRD pattern gives a crystallite size of 48 nm with a standard error of 5.2 nm; this being a volume-average size distribution is not directly comparable to the number-average size distribution given above from TEM measurements. Converting the TEM size data to a volume-averaged basis gives a value of 46 nm. Therefore, the XRD size and the TEM size agree to within the errors of the measurements, indicating that the resulting nanocubes are single-crystal domains. However, stacking faults are quite prevalently observed as indicated in Figure 1. Details of the Scherrer analysis are given in the methodology section.

Raman spectroscopy has also been utilized for structural analysis, with the results reported in Figure 3B. All five Raman active modes for pyrite result from vibrations of the sulfur atoms with stationary iron,

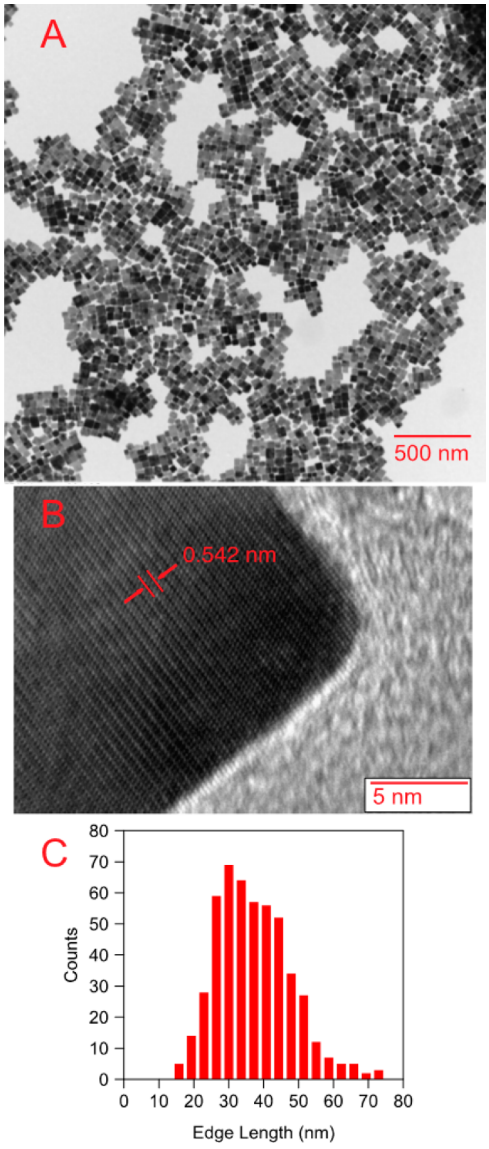

Figure 2. (A) TEM image of the synthesized FeS_2 nanocubes showing the sample morphology and size distribution, and (B) HRTEM image showing lattice fringes with a measured d-spacing corresponding to the FeS_2 {100} lattice planes. In (C) the particle size distribution (number distribution) is determined from TEM measurements.

so this characterization method gives high-resolution information about the chemical environment of the S_2

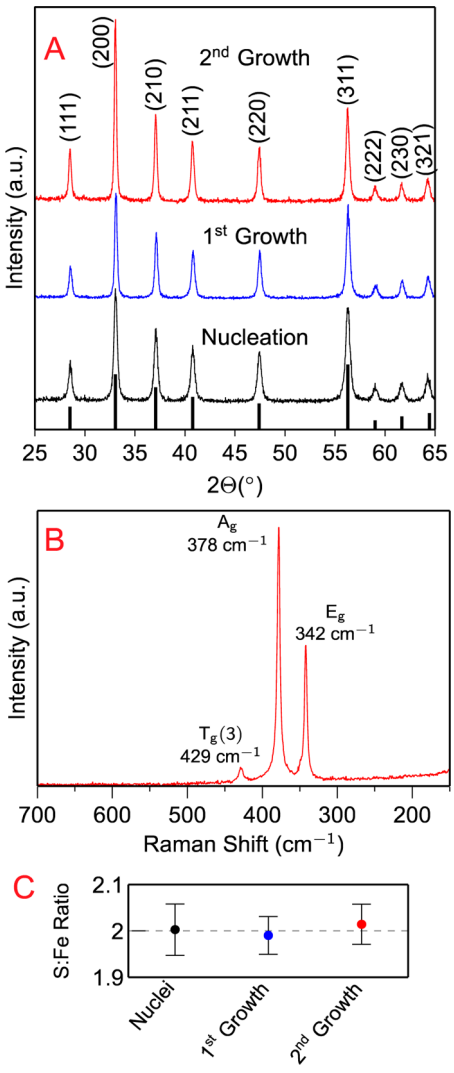

Figure 3. (A) Powder XRD of FeS_2 product through the nucleation and growth stages with JCPDS card no. 06-0710 for reference. (B) Raman spectra of the final FeS_2 nanocubes with modes indexed. (C) Elemental analysis with energy-dispersive X-ray spectroscopy through the nucleation and growth stages.

units.[30] In this analysis we have used $\lambda = 532$ nm for excitation; at this wavelength pyrite is highly absorbing, with an absorption coefficient of $\sim 4 \times 10^5$ cm^{-1}.[5,31] This excitation wavelength gives a penetration depth typical for metals, not semiconductors, and as a consequence, much of the Raman scattering reaching the detector results from the near surface of the material.

This Raman analysis gives three peaks, which have previously been indexed to different stretching and librational modes of the persulfide units and show close correspondence.[32] Also, the $T_g(3)$ mode is a mixture of stretching and librational motion of four adjacent S_2 units, and the relative strength of this mode has been argued as indicating good long-range order in the crystal.[33] Additionally, there is a small shoulder on the E_g mode at ~ 350 cm^{-1}. This shoulder has been ascribed to the $T_g(1)$ mode, which to our knowledge has been observed only by using polarized light (to block out the overlapping E_g mode)[34] or a liquid-nitrogen-cooled CCD.[30] Peaks sharp enough for the observation of this mode are taken to indicate the chemically homogeneous nature of the product.

Energy-dispersive X-ray spectroscopy was utilized to analyze the elemental composition of the product through each of the growth cycles. The ratio of sulfur to iron remained stoichiometric within the experimental accuracy of the method for all three synthetic stages.

Optical and Electronic Properties. The use of UV–vis absorption spectroscopy to analyze the electronic structure of the pyrite nanocubes gave unexpected results. The as-prepared nanocubes agglomerated quickly; we were unable to keep them rigorously dispersed during the cleaning process. Therefore, to obtain a stable dispersion for analysis, we sonicated the solution with excess oleylamine (following the procedure described by Li *et al.*).[28] During this procedure, it was observed that the agglomerated black solution would turn purple/red in color and the optical density would increase as the nanocubes became more dispersed. As is normally observed for agglomerated nanoparticles, nanocubes that were less dispersed (*i.e.*, not sonicated as long or with less oleylamine) had a significant UV–vis scattering tail, that is, higher absorption at longer wavelengths compared with more dispersed samples, as shown in Figure 4A. Unexpectedly however, Figure 4A also shows that these solutions of small agglomerates of nanocubes have more distinct excitonic features at ~300 and ~500 nm, in addition to the scattering tail. This phenomenon can be understood as a signal resulting from resonant light scattering (RLS). RLS is greatly enhanced light scattering that occurs when agglomerated chromophores are irradiated by light with a wavelength in close proximity to an electronic transition of the chromophore.[35] Despite the seldom-used terminology in this discipline, pyrite could certainly be termed a chromophore given its high absorption coefficient. Further, TEM images have often shown the propensity for these nanocubes to agglomerate in a face-sharing orientation. To investigate this further, the common test for RLS was conducted, which uses a fluorimeter in a 90° configuration with synchronously scanning excitation and emission monochromators.[36] Figure 4B shows distinctly increased light scattering at the two electronic transitions in question, persuasively implicating RLS as the cause of the distinct excitonic peaks in the less dispersed UV–vis spectrum shown in Figure 4A. Although RLS has been observed for metal nanoparticles[37] (often involving surface plasmon resonance as well) and semiconductor structures grown by molecular beam epitaxy,[38] no previous work has been identified by us where a significant RLS signal has been shown to result between semiconductor nanocrystals.

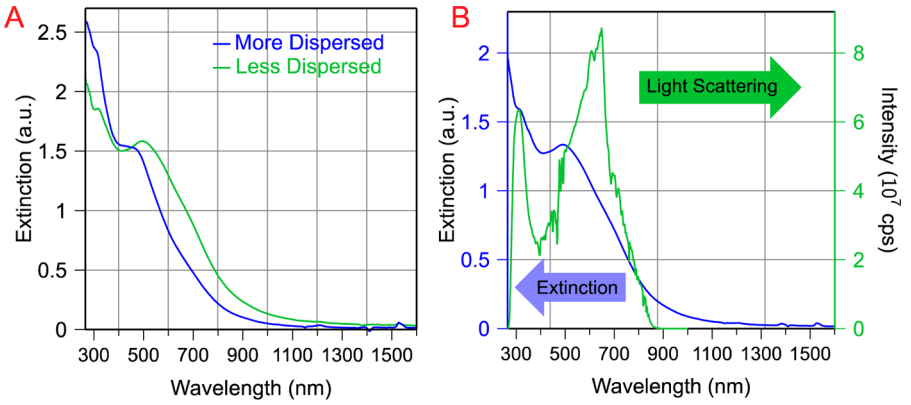

Figure 4. (A) Absorption spectroscopy of identical nanocube solutions that differ only in how long they were sonicated prior to analysis. (B) The resulting RLS spectrum (green) produced by synchronously scanning excitation and emission monochromators on a fluorimeter, plotted along with the previously measured absorption spectrum (blue) of that nanocube sample.

Given that RLS is an unusual explanation for the observed optical properties, it is important to constrain the chemical processes at work as best as possible. To this end, we are cautioned by the fact that previous studies have demonstrated that storage of some types of nanoparticles ($CuInSe_2$, for example) in excess alkylamines results in etching of the particles over time.[39] To understand if this is happening in this case, we have imaged nanocubes by TEM on the day of synthesis and after 17 days in chloroform with excess oleylamine (Figure S1, Supporting Information,). No change in size or morphology is evident. We therefore believe that sonication with excess alkylamine results in dispersions without bulk chemical changes to the particles. However, detailed analysis of amine surface bonding dynamics, and the resulting affect on RLS, remains to be evaluated.

While RLS in solution does not give new information about the electronic structure of pyrite, it does indicate that electronic coupling between nanocubes is readily achieved, to the point of being nearly unavoidable. Given that so much effort has been undertaken recently to make conductive nanocrystal films, this phenomenon may point to the amenability of this material to produce films with high electron mobilities. Of note, theoretical work indicates that the coupling energy between nanocubes is a factor of 3 higher than for spheres, given increased wave function overlap.[40]

Studies have proposed ways to deconvolute the extinction spectrum of an RLS-affected sample into scattering and absorption signals.[37] However, in order to obtain a signal from only absorption, we have dispersed these nanocubes in octadecylamine, which we have shown can sterically hinder RLS to an insignificant level (Figure S2, Supporting Information). In Figure 5A UV−vis absorption spectra are given for the nucleation and both growth steps and are now labeled as absorbance rather than extinction as in Figure 4. These data indicate similar electronic behavior of the as-nucleated nanocrystals and rationally grown nanocubes. However, they also indicate that growing the nanocubes causes decreased absorption at high-energy wavelengths (~255−350 nm) and, to a lesser extent, increased absorption in the visible and near-infrared (~550−1000 nm).

In order to further understand the differences in the three spectra given in Figure 5A, we have compared the experimental results obtained here (after the final growth step) with the theoretical data of Vadkhiya and Ahuja.[31] Specifically, we have converted the absorbance data to absorption coefficient (α) and, not knowing the exact path length for the incident radiation in our experiment, normalized it to their data in Figure 5B. These two data sets show remarkably close correspondence. Compared to the data shown in Figure 5B, absorption for the as-nucleated and first growth steps is anomalously large at 255−350 nm (*i.e.*, above ~3.5 eV). Conversely, the final nanocube product shows higher absorption in the 550−1000 nm range compared with the nucleation and first growth products. While a much smaller affect, this absorption character of the final nanocubes is again closer to the theoretical data than that of the nucleation or first growth products. Lastly, as the synthesis proceeds, the absorption peaks at ~440 and ~310 nm become more pronounced. These absorption differences may therefore be important in indicating the relative shape and/or surface perfection of the product.

Figure 5C gives $(A\hbar\omega)^n$ for the final nanocube product as a function of the energy of incident radiation, with $n = 1/2$ for indirect transitions and $n = 2$ for direct ones. Linear behavior is observed, indicating an indirect transition at ~1.1 eV. The two excitonic features can also be approximated as transitions occurring at ~1.9 and ~3.0 eV.

This 1.1 eV band gap is slightly higher than the accepted experimental value of 0.95 eV. Of note, recent theoretical calculations also give a slightly higher band gap (1.02 eV).[12,14] However, the analysis given here assumes the existence of parabolic bands, which may be a poor assumption for modeling pyrite's quite flat

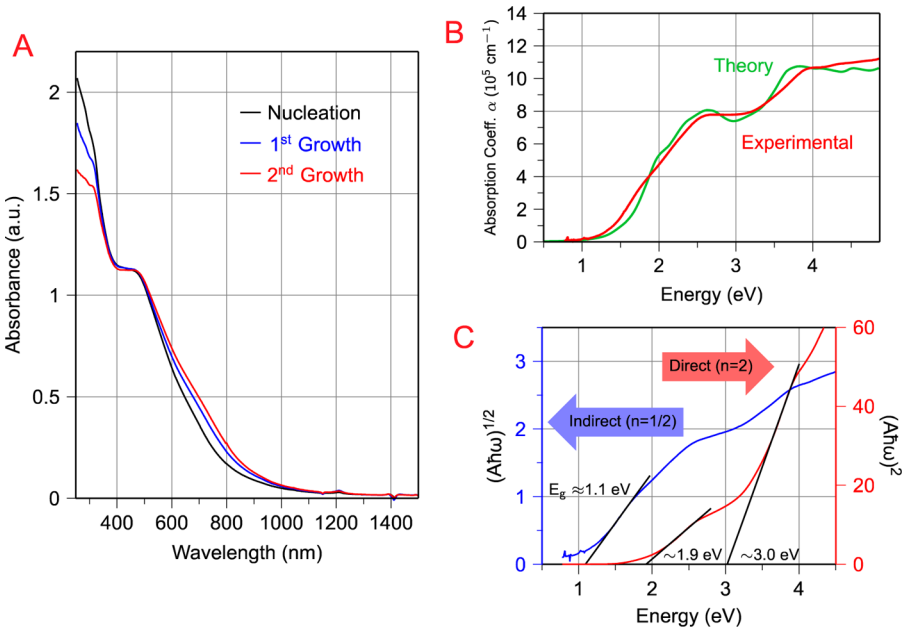

Figure 5. (A) UV−vis absorption spectroscopy of pyrite plotted for the nucleation and both growth steps. (B) Absorption spectroscopic data for the final product normalized to density functional theory results from Vadkhiya and Ahuja.[31] (C) Band-edge absorption of the final product assuming indirect (n = 1/2) and direct (n = 2) absorption character.

bands.[5] Therefore, the data approximated in this way agree with both previous experimental and theoretical data within the errors of the approximation. The two direct transitions can be tentatively indexed to interband transitions as given by the imaginary part of the dielectric constant in the theoretical works of Vadkhiya and Ahuja[31] and Antonov *et al.*[41] The 1.9 eV transition reported here is quite close to their calculations of 2 and 2.1 eV, respectively. However, the 3.0 eV second direct transition is ~15% less than their assignments of 3.6 and 3.5 eV, respectively. This difference may arise from the ambiguity of the proper level of absorption in this energy region, as described above.

Reaction Mechanism and Kinetics. As compared to other binary transition metal chalcogenides, the synthesis of dichalcogenides with the pyrite structure has proven problematic. This difficulty stems from the notion that no common precursor molecule decomposes to give the S_2^{2-} unit (or singly charged sulfide radicals). This may be because the S−S bond at ~265 kJ/mol is weak in comparison with common organosulfur bonds.[42] Fortunately, a large body of information on pyrite nucleation and growth comes from the earth science community. Given the lack of S_2^{2-} precursor ions, pyrite does not form directly from monomer in solution but goes through an FeS intermediate,[43] a feature common to synthetic reactions as well.[25] Rapid nucleation of iron monosulfides seems to prevent a sufficiently high supersaturation for an adequate FeS_2 nucleation, often causing large sizes as a result.[44] Conversely, the slow dissolution of iron monosulfides creates reaction-controlled growth conditions, which can cause the euhedral facets of pyrite often observed.[25,28,45]

In addition to involving a precipitated reaction intermediate, we believe that pyrite precipitation can be considered an irreversible reaction. This has been shown by others who have indicated that hot-injection produces many nuclei that grow by agglomeration[27] and that higher concentrations lead to smaller particles,[28] indicating a kinetically controlled reaction (see Shevchenko *et al.*,[46] for example, for the attendant theory). To add to this body of evidence, even though we have grown these nanocubes over a period of many hours, Ostwald ripening has not been observed.

In this study alkylamines have been used, which are thought to be relatively weak ligands to semiconductor particles.[47] It is our conjecture that a relatively weak ligand is necessary in order that the FeS reaction intermediate is not isolated. Further, even if a ligand is not strong enough to isolate FeS, the slow dissolution of well-ligated FeS will create >100 nm sizes of FeS_2,[25] larger than is the goal of this synthesis. Therefore, concerning the size of the nucleation product, we are constrained by wanting small particles but lacking the ability to vary the bond strength of the ligand to the final precipitated phase. However, monomer kinetics can still be altered significantly by varying the concentration and/or chain length of the ligands.[48] Lowering the reactivity of the monomer by ligand concentration and chain length is caused by steric factors, which will favor nucleation over growth, given that growth involves longer range transport of monomer through the synthesis. Thus size control can be mediated by interligand interactions, which is the theoretical basis for the following analysis.

Given the foregoing constraints and the motivation for small (<50 nm) particles described above, we have

chosen to nucleate in pure hexadecylamine (C16), which has strong interligand interactions given the long length of the alkane tail, to force the creation of small particles despite the slow dissolution of FeS. This has resulted in a mixture of cubic and completely irregular particles, as shown in the left side of Figure 1. Such a kinetically constrained nucleation necessarily prevents an optimal shape and surface, causing us to add oleylamine (C18), which has been shown to act like octylamine (C8) given its cis configuration,[49] for the rational growth steps of the synthetic process. If no additional oleylamine is added and the existing hexadecylamine is used as the solvent for the growth steps, the product will be more irregular in shape (Figure S3, Supporting Information). We believe this indicates conditions in which the limiting step to particle growth is monomer reaching the surface of the particle. Given that this reaction is considered irreversible, this leads to conditions in which particle shape does not evolve rationally. Conversely, the well-faceted nanocubes shown in Figures 1 and 2 indicate that the limiting step to nanocube growth with oleylamine added is the reaction of monomer with the crystal surface, giving the reaction-controlled conditions necessary to form euhedral facets.

Hexadecylamine has been used for nucleation instead of octadecylamine (C18) because, in the latter case, a more polydisperse product was observed with a large quantity of particles with irregular shape (Figure S4, Supporting Information). It is possible that the ligand−ligand interaction of octadecylamine is so strong at 200 °C (the growth temperature) that it becomes difficult for it to be in the "off" position often enough to allow for rational growth.[47]

Controlling Shape by Sulfur Chemical Potential. As described above, ligand conditions were changed between the nucleation and growth stages to allow for reaction-controlled growth. However, reaction-controlled conditions are necessary, but not sufficient, to grow particles of a particular terminal face. For sufficiency it is also necessary to control the chemical potentials of the reacting constituents so as to affect their individual rates of adsorption onto specific crystal facets.

Theoretical work has elucidated the energetic differences between various common surface terminations as a function of sulfur chemical potential within the reaction conditions.[16,50] These studies have found that {100} faces attain the lowest energy at sulfur-poor/iron-rich conditions, with the {210} and {111} faces becoming preferred as conditions become increasingly sulfur rich, successively. These results have been used as the "handle" with which to control the shape of the particles, using a lower concentration, and therefore chemical potential, of sulfur (relative to Fe chemical potential) during the growth of the preformed irregular nuclei. Specifically, [S]/[Fe] = 6 for the nucleation stage was decreased to [S]/[Fe] = 2.05 for the growth stages. In this way, the altered chemical potential of sulfur was used as a driving force to grow all other faces besides {100} to extinction.

When grown at [S]/[Fe] = 2, it was found that some pyrrhotite FeS was isolated (Figure S5, Supporting Information). This can be explained by reference to the iron−sulfur binary phase diagram,[51] where, if any H_2S evaporated (which is known to form in this reaction),[52] resulting in a loss of sulfur from the system, then thermodynamic considerations will predict a mixture of pyrite and pyrrhotite. Therefore, slightly excess sulfur has been used beyond what would seem to be ideal for promoting cubic faces. If the sulfur concentration is increased further ([S]/[Fe] = 2.1, Figure S6, Supporting Information), it is observed that the edges of the resulting particles become slightly more rounded than for [S]/[Fe] = 2.05, indicating the sensitivity of this method to shape control.

It is interesting to note that despite pyrite being a cubic crystal system, and our attempts to create "nanocubes" as described in the preceding paragraph, many of the crystals actually have rectangular dimensions, as shown in Figure 1. This may be due, in part, to agglomeration during the nucleation stage. However, it seems to be a seldom-commented fact that the ⟨100⟩ crystallographic directions of pyrite are not interchangeable and display only 2-fold symmetry.[43] Therefore, it might also be due to different reaction rates on distinct {100} faces. Which {100} faces may be forming the larger and smaller area facets of these "nanocuboids" has not been evaluated in this study. Studies exploiting the chiral nature of this material may be interesting in the future.

Additional Reaction Considerations. The focusing of the size distribution in this synthesis is unusual in the large size of the growth stages, specifically $[Fe]_{grow}/[Fe]_{nuc} = 2$. More concentrated growth conditions have been shown to result in some smaller particles, indicating a secondary nucleation (Figure S7, Supporting Information). However, as can be seen in Figure 1, after the first growth step there are still some truncated cubes with either {210} or {111} faces. Therefore, a second growth phase has been employed, again at $[Fe]_{grow}/[Fe]_{nuc} = 2$, to create more perfectly terminated nanocubes. Theoretically, the growth rate of a particle decreases linearly as the size of the particle increases if the experiment is reaction controlled, allowing the size-focusing shown in Figure 1.[53] Additionally, there has been significant interest lately in using continuous monomer production to focus size distributions by keeping the amount of monomer above a level that allows Ostwald ripening.[54] Although we think that the irreversible nature of this reaction prevents Ostwald ripening, this study can be considered an extreme example of monomer production from the slow dissolution of FeS.

Despite the focus of this work in maintaining the semiconducting properties of pyrite, the procedure, being a noninjection synthesis, also makes it more amenable to scale-up and more reproducible than the hot-injection syntheses previously reported. Additionally, herein the metal chloride has not been dissolved in the alkylamine prior to the introduction of the sulfur, as is standard with this type of synthesis, further streamlining the synthetic process. Also, because of the large amounts of monomer added to the reaction, we have chosen to cool the reaction and allow it to freeze rather than injecting additional chemical species at the growth temperature. We believe that this approach makes the synthetic protocol significantly easier to undertake, less time sensitive, and more reproducible.

In addition to shape considerations, as described above, the control of the relative perfection of surfaces is important to the study of pyrite. Obviously the conditions for the best shape control might be quite different from those of optimal surface termination. There is a well-developed body of work in perfecting the surfaces of spherical nanocrystals so that their photoluminescent efficiency is maximized. The "bright point" of an ensemble of particles in a synthesis has been shown to occur when the surfaces of the particles are in diffusive equilibrium with the surrounding monomer, allowing time for optimal surface reconstruction.[55−57] As described above, we believe this reaction can be considered irreversible. Therefore, it is not possible to use the foregoing logic of diffusive equilibrium. Instead, the use of relatively low temperatures (200 °C) over long reaction times may allow for rational surface growth in addition to its effect on crystal shape. This conjecture is being actively tested in ongoing work in our laboratory.

CONCLUSION

We present a synthesis of iron pyrite (FeS_2) nanocubes in an attempt to address the fundamental problems inherent to the material. Specifically, by creating strong interligand interactions we have succeeded in decreasing growth kinetics and thereby nucleating small nanoparticles despite a necessarily small supersaturation (given the precipitation and slow dissolution of FeS). We have then decreased the interligand interactions to allow for more rational growth, now limited by the interaction of sulfur with the growing pyrite surface. Specifically, we have isolated $\{100\}$ faces by lowering the sulfur chemical potential of the reaction; this validates theoretical considerations that argue that $\{100\}$ faces become lowest in energy in sulfur-poor/iron-rich conditions. The resulting product has an average edge length of ∼37 nm, making it smaller than previous syntheses of nanoscale cubic pyrite. This may allow the design of pyrite thin films with thicknesses more closely corresponding to the absorption coefficient of the material. The product has been shown to have unusual electronic properties including a strong resonant light scattering signal, indicating the ease with which electronic coupling occurs between particles. Shape-engineered nanocubes are shown to have different electromagnetic absorption properties than irregular nanocrystals, with the nanocube product demonstrating behavior closer to that produced by theoretical calculations. The resulting nanocube product may therefore be amenable to maintaining semiconducting behavior for applications.

METHODS

The synthetic scheme employed heats anhydrous $FeCl_2$ and elemental sulfur in alkylamines. This chemical route has recently become somewhat standard in pyrite syntheses[25,27,28] and is an adaptation of the original method pioneered by Joo *et al.*[58] A 0.5 mmol (63.4 mg) amount of anhydrous $FeCl_2$ beads, 10 g of hexadecylamine, and 3 mmol (96.2 mg) of S flakes were brought to 250 °C for 3 h in a 50 mL three-neck flask under argon atmosphere with magnetic stirring at 240 rpm. Uncommonly, this is a so-called "heating up" synthesis, and the Fe−Cl−amine complex that is usually formed previous to reaction with sulfur was not formed here.[25,58]

After the nucleation reaction was completed, the flask was allowed to cool naturally and the raw solution allowed to freeze with the hexadecylamine. Once room temperature was obtained, 1 mmol (126.8 mg) of $FeCl_2$, 2.05 mmol (65.7 mg) of S, and 15 mL of oleylamine were added through one of the necks of the flask with argon flowing over the frozen solution (*warning*: *oleylamine can cause chemical burns*). The flask was then resealed and brought to 200 °C for 9 h, stirring at 750 rpm. This growth process was performed a second time except without the addition of more oleylamine (*i.e.*, only $FeCl_2$ and sulfur). Upon completion of the second growth step, ∼10 mL of chloroform was added and the solution was lightly centrifuged (2000 rpm for 1 min) followed by decanting of the supernatant. The precipitate was cleaned twice in chloroform by redispersion and centrifugation and was subsequently stored in chloroform for analysis.

TEM images were acquired with a Philips CM100 with a 100 kV accelerating voltage and a bottom-mounted digital camera. Samples were prepared by immersing a carbon-coated TEM grid into a nanocube solution in chloroform for about a second and then drying in air; this was done immediately prior to analysis to avoid oxidation ambiguity. HRTEM images were acquired under the same procedure with a Philips CM200 operated at 200 kV.

XRD analysis was conducted on a Scintag PAD5 XRD using a Cu K-alpha X-ray source (λ = 0.154056 nm) accelerated by a 40 kV voltage. For analysis a nanocube sample in solution was pipetted onto a glass slide, and the chloroform was allowed to evaporate. The slide was rotated at 0.12°/min relative to the detector in a reflection (*i.e.*, Bragg−Brentano) geometry.

The Scherrer equation to measure pXRD peak broadening is

$$D = \frac{K\lambda}{B\cos\vartheta}$$

It is well known that deciding on an appropriate Scherrer constant (K) is a difficult task. Stokes and Wilson computed K values for various reflections for cubic-shaped crystals with a

cubic crystal system.[59] They used the integral breadth definition as the measure of the width of the diffraction peaks (*i.e.*, the value of B). This measure is defined as the area under the peak in question divided by its peak intensity. To use their Scherrer constants, we have followed this definition (instead of full width at half-maximum (fwhm)). To use their *K* values we have also defined *D* as the cube root of the nanocube volume, rather than the more standard definition where *D* is the crystallite size in the direction perpendicular to the lattice planes.

With these definitions, the size of the crystallite domains of the particles have been evaluated for the (111), (200), (210), (211), (220), and (311) reflections, with the reported result being an average of the six. Standard error is given as the standard deviation of these six measurements. These data are given in Table S1 (Supporting Information). Instrumental peak broadening was estimated by analyzing a sample of microcrystalline quartz.

Raman spectra were collected on a Jasco NRS-3100 using a 532 nm laser for excitation. An OD2 filter was used, allowing the sample to be irradiated by 0.7 mW. Raman scattering was dispersed by a 2400 lines/mm grating. The CCD was cooled by a Peltier element, which kept it at −58 °C. For analysis a nanocube sample in solution was pipetted onto a glass slide, and the chloroform was allowed to evaporate. The sample was analyzed under 100× magnification.

Fluorimeter measurements were conducted on a Horiba Fluorolog-3 fluorimeter. The analysis was performed in chloroform or trichloroethylene in a 1 cm quartz cuvette. As described above, the analysis involved simultaneously scanning the excitation and emission monochromators. The emission monochromator is at a 90° orientation to the excitation. It was found that 3 nm slits for both excitation and emission monochromators gave the best signal. The signal was obtained as the ratio of emission per lamp intensity (S/R). The signal was background corrected by running an identical experiment with just the solvent and cuvette system.

Ultraviolet−visible (UV−vis) measurements were conducted on a Varian Cary 500 spectrophotometer. Samples were analyzed in chloroform with a double-beam configuration and 1 nm data collection interval.

Energy-dispersive X-ray spectroscopy (EDX) was performed on a JEOL JSM-6480LV scanning electron microscope equipped with an INCA PentaFET x3 EDX spectrometer. Samples were mounted on an aluminum stub with carbon tape and irradiated with an electron source set at 15 kV. For each data point three to six large-area (>2 um^2) spectra were taken, and the results averaged.

Conflict of Interest: The authors declare no competing financial interest.

Acknowledgment. The authors gratefully acknowledge primary support provided by the University of Colorado at Boulder's Innovative Seed Grant Program, with ancillary support provided by DARPA Defense Sciences Office Grant No. FA8650-08-1-7839. We are grateful to L. Vadkhiya and B. L. Ahuja for providing their theoretical optical absorption data.

Supporting Information Available: Materials and optical details and additional RLS, XRD, TEM, and Scherrer analysis data are given. This material is available free of charge *via* the Internet at http://pubs.acs.org.

REFERENCES AND NOTES

1. Shao-Horn, Y.; Osmialowski, S.; Horn, Q. Nano-FeS_2 for Commercial Li/FeS_2 Primary Batteries. *J. Electrochem. Soc.* **2002**, *149*, A1499–A1502.
2. Yersak, T.; Macpherson, H. A.; Kim, S. C.; Le, V. D.; Kang, C. S.; Son, S. B.; Kim, Y. H.; Trevey, J.; Oh, K. H.; Stoldt, C.; *et al.* Solid State Enabled Reversible Four Electron Storage. *Adv. Energy Mater.*, in press.
3. Burton, J. D.; Tsymbal, E. Y. Highly Spin-Polarized Conducting State at the Interface Between Nonmagnetic Band Insulators: $LaAlO_3$/FeS_2 (001). *Phys. Rev. Lett.* **2011**, *107*, 166601.
4. Evangelou, V. P.; Zhang, Y. L. A Review - Pyrite Oxidation Mechanisms and Acid-Mine Drainage Prevention. *Crit. Rev. Environ. Sci. Technol.* **1995**, *25*, 141–199.
5. Ferrar, I.; Nevskaia, D.; Delasheras, C.; Sanchez, C. About the Band-Gap Nature of FeS_2 as Determined from Optical and Photoelectrochemical Measurements. *Solid State Commun.* **1990**, *74*, 913–916.
6. Wadia, C.; Alivisatos, A. P.; Kammen, D. M. Materials Availability Expands the Opportunity for Large-Scale Photovoltaics Deployment. *Environ. Sci. Technol.* **2009**, *43*, 2072–2077.
7. Ennaoui, A.; Fiechter, S.; Pettenkofer, C.; Alonsovante, N.; Büker, K.; Bronold, M.; Höpfner, C.; Tributsch, H. Iron Disulfide for Solar-Energy Conversion. *Sol. Energy Mater. Sol. Cells* **1993**, *29*, 289–370.
8. Hodes, G.; Cahen, D. All-Solid-State, Semiconductor-Sensitized Nanoporous Solar Cells. *Acc. Chem. Res.* **2012**, *45*, 705–713.
9. Dasbach, R.; Willeke, G.; Blenk, O. Iron Sulfide for Photovoltaics. *MRS Bull.* **1993**, *18*, 56–60.
10. Yu, L.; Lany, S.; Kykyneshi, R.; Jieratum, V.; Ravichandran, R.; Pelatt, B.; Altschul, E.; Platt, H. A. S.; Wager, J. F.; Keszler, D. A.; *et al.* Iron Chalcogenide Photovoltaic Absorbers. *Adv. Energy Mater.* **2011**, *1*, 748–753.
11. Sun, R.; Chan, M. K. Y.; Kang, S. Y.; Ceder, G. Intrinsic Stoichiometry and Oxygen-Induced P-Type Conductivity of Pyrite FeS_2. *Phys. Rev. B* **2011**, *84*, 035212.
12. Hu, J.; Zhang, Y.; Law, M.; Wu, R. First-Principles Studies of the Electronic Properties of Native and Substitutional Anionic Defects in Bulk Iron Pyrite. *Phys. Rev. B* **2012**, *85*, 085203.
13. Ellmer, K.; Höpfner, C. On the Stoichiometry of the Semiconductor Pyrite (FeS_2). *Philos. Mag. A* **1997**, *75*, 1129–1151.
14. Sun, R.; Chan, M.; Ceder, G. First-Principles Electronic Structure and Relative Stability of Pyrite and Marcasite: Implications for Photovoltaic Performance. *Phys. Rev. B* **2011**, *83*, 235311.
15. Murphy, R.; Strongin, D. R. Surface Reactivity of Pyrite and Related Sulfides. *Surf. Sci. Rep.* **2009**, *64*, 1–45.
16. Alfonso, D. R. Computational Investigation of FeS_2 Surfaces and Prediction of Effects of Sulfur Environment on Stabilities. *J. Phys. Chem. C* **2010**, *114*, 8971–8980.
17. Andersson, K.; Nyberg, M.; Ogasawara, H.; Nordlund, D.; Kendelewicz, T.; Doyle, C.; Brown, G.; Pettersson, L.; Nilsson, A. Experimental and Theoretical Characterization of the Structure of Defects at the Pyrite FeS_2(100) Surface. *Phys. Rev. B* **2004**, *70*, 195404.
18. Zhang, Y.; Hu, J.; Law, M.; Wu, R. Q. The Effect of Surface Stoichiometry on the Band Gap of the Pyrite FeS_2 (100) Surface. *Phys. Rev. B* **2012**, *85*, 085314.
19. Nair, N. N.; Schreiner, E.; Marx, D. Glycine at the Pyrite-Water Interface: the Role of Surface Defects. *J. Am. Chem. Soc.* **2006**, *128*, 13815–13826.
20. Rosso, K.; Becker, U.; Horchella, M. Surface Defects and Self-Diffusion on Pyrite {100}: an Ultra-High Vacuum Scanning Tunneling Microscopy and Theoretical Modeling Study. *Am. Mineral.* **2000**, *85*, 1428–1436.
21. Nesbitt, H.; Bancroft, G.; Pratt, A.; Scaini, M. Sulfur and Iron Surface States on Fractured Pyrite Surfaces. *Am. Mineral.* **1998**, *83*, 1067–1076.
22. Ennaoui, A.; Fiechter, S.; Jaegermann, W.; Tributsch, H. Photoelectrochemistry of Highly Quantum Efficient Single-Crystalline N-FeS_2 (Pyrite). *J. Electrochem. Soc.* **1986**, *133*, 97–106.
23. Liu, C.; Pettenkofer, C.; Tributsch, H. Enhancement of Photoactivity in Pyrite (FeS_2) Interfaces by Photoelectrochemical Processes. *Surf. Sci.* **1988**, *204*, 537–554.
24. Elsetinow, A.; Guevremont, J.; Strongin, D. R.; Schoonen, M. A. A.; Strongin, M. Oxidation of {100} and {111} Surfaces of Pyrite: Effects of Preparation Method. *Am. Mineral.* **2000**, *85*, 1428–1436.
25. Bi, Y.; Yuan, Y.; Exstrom, C. L.; Darveau, S. A.; Huang, J. Air Stable, Photosensitive, Phase Pure Iron Pyrite Nanocrystal Thin Films for Photovoltaic Application. *Nano Lett.* **2011**, *11*, 4953–4957.

26. Wadia, C.; Wu, Y.; Gul, S.; Volkman, S. K.; Guo, J.; Alivisatos, A. P. Surfactant-Assisted Hydrothermal Synthesis of Single Phase Pyrite FeS_2 Nanocrystals. *Chem. Mater.* **2009**, *21*, 2568–2570.
27. Puthussery, J.; Seefeld, S.; Berry, N.; Gibbs, M.; Law, M. Colloidal Iron Pyrite (FeS_2) Nanocrystal Inks for Thin-Film Photovoltaics. *J. Am. Chem. Soc.* **2011**, *133*, 716–719.
28. Li, W.; Doeblinger, M.; Vaneski, A.; Rogach, A. L.; Jaeckel, F.; Feldmann, J. Pyrite Nanocrystals: Shape-Controlled Synthesis and Tunable Optical Properties *Via* Reversible Self-Assembly. *J. Mater. Chem.* **2011**, *21*, 17946–17952.
29. Paszkowicz, W.; Leiro, J. Rietveld Refinement Study of Pyrite Crystals. *J. Alloys Compd.* **2005**, *401*, 289–295.
30. Kleppe, A.; Jephcoat, A. High-Pressure Raman Spectroscopic Studies of FeS_2 Pyrite. *Mineral. Mag.* **2004**, *68*, 433–441.
31. Vadkhiya, L.; Ahuja, B. L. Electronic and Optical Properties of Iron Pyrite. *J. Alloys Compd.* **2011**, *509*, 3042–3047.
32. Sourisseau, C.; Cavagnat, R. The Vibrational Properties and Valence Force Fields of FeS_2, RuS_2 Pyrites and FeS_2 Marcasite. *J. Phys. Chem. Solids* **1991**, *52*, 537–544.
33. Teo, M. Y. C.; Kulinich, S. A.; Plaksin, O. A.; Zhu, A. L. Photo-induced Structural Conversions of Transition Metal Chalcogenide Materials. *J. Phys. Chem. A* **2010**, *114*, 4173–4180.
34. Vogt, H.; Chattopadhyay, T. Complete First-Order Raman Spectra of the Pyrite Structure Compounds FeS_2, MnS_2 And SiP_2. *J. Phys. Chem. Solids* **1983**, *44*, 869–873.
35. Pasternack, R.; Collings, P. Resonance Light-Scattering - a New Technique for Studying Chromophore Aggregation. *Science* **1995**, *269*, 935–939.
36. Lu, W.; Band, B. S. F.; Yu, Y.; Li, Q. G.; Shang, J. C.; Wang, C.; Fang, Y.; Tian, R.; Zhou, L. P.; Sun, L. L.; *et al.* Resonance Light Scattering and Derived Techniques in Analytical Chemistry: Past, Present, and Future. *Microchim. Acta* **2007**, *158*, 29–58.
37. Micali, N.; Mallamace, F.; Castriciano, M.; Romeo, A.; Scolaro, L. Separation of Scattering and Absorption Contributions in UV/Visible Spectra of Resonant Systems. *Anal. Chem.* **2001**, *73*, 4958–4963.
38. Gurioli, M.; Bogani, F.; Ceccherini, S.; Vinattieri, A.; Colocci, M. Resonant Elastic Light Scattering and Coherence Relaxation in Semiconductor Structures. *J. Opt. Soc. Am. B* **1996**, *13*, 1232–1240.
39. Koo, B.; Patel, R. N.; Korgel, B. A. Synthesis of $CuInSe_2$ Nanocrystals with Trigonal Pyramidal Shape. *J. Am. Chem. Soc.* **2009**, *131*, 3134–3135.
40. Liljeroth, P.; Overgaag, K.; Urbieta, A.; Grandider, B.; Hickey, S. G.; Vanmaekelbergh, D. Variable Orbital Coupling in a Two-Dimensional Quantum-Dot Solid Probed on a Local Scale. *Phys. Rev. Lett.* **2006**, *97*, 096803.
41. Antonov, V. N.; Germash, L. P.; Shpak, A. P.; Yaresko, A. N. Electronic Structure, Optical and X-Ray Emission Spectra in FeS_2. *Phys. Status Solidi B* **2009**, *246*, 411–416.
42. Cotton, F. A. *Advanced Inorganic Chemistry*, 6th ed.; Wiley-Interscience, 1999; p 499.
43. Rickard, D.; Luther, G. W. Chemistry of Iron Sulfides. *Chem. Rev.* **2007**, *107*, 514–562.
44. Schoonen, M.; Barnes, H. Reactions Forming Pyrite and Marcasite From Solution 1. Nucleation of FeS_2 below 100C. *Geochim. Cosmochim. Acta* **1991**, *55*, 1495–1504.
45. Wang, D. W.; Wang, Q. H.; Wang, T. M. Controlled Growth of Pyrite FeS_2 Crystallites by a Facile Surfactant-Assisted Solvothermal Method. *CrystEngComm* **2010**, *12*, 755–761.
46. Shevchenko, E.; Talapin, D.; Schnablegger, H.; Kornowski, A.; Festin, Ö.; Svedlindh, P.; Haase, M.; Weller, H. Study of Nucleation and Growth in the Organometallic Synthesis of Magnetic Alloy Nanocrystals: The Role of Nucleation Rate in Size Control of $CoPt_3$ Nanocrystals. *J. Am. Chem. Soc.* **2003**, *125*, 9090–9101.
47. Pradhan, N.; Reifsnyder, D.; Xie, R.; Aldana, J.; Peng, X. Surface Ligand Dynamics in Growth of Nanocrystals. *J. Am. Chem. Soc.* **2007**, *129*, 9500–9509.
48. Yu, W.; Wang, Y.; Peng, X. Formation and Stability of Size-, Shape-, and Structure-Controlled CdTe Nanocrystals: Ligand Effects on Monomers and Nanocrystals. *Chem. Mater.* **2003**, *15*, 4300–4308.
49. Dumestre, F.; Chaudret, B.; Amiens, C.; Fromen, M. C.; Casanove, M. J.; Renaud, P.; Zurcher, P. Shape Control of Thermodynamically Stable Cobalt Nanorods Through Organometallic Chemistry. *Angew. Chem., Int. Ed.* **2002**, *41*, 4286–4289.
50. Barnard, A. S.; Russo, S. P. Modelling Nanoscale FeS_2 Formation in Sulfur Rich Conditions. *J. Mater. Chem.* **2009**, *19*, 3389–3394.
51. Walder, P.; Pelton, A. Thermodynamic Modeling of the Fe-S System. *J. Phase Equilib. Diffus.* **2005**, *26*, 23–38.
52. Thomson, J. W.; Nagashima, K.; Macdonald, P. M.; Ozin, G. A. From Sulfur–Amine Solutions to Metal Sulfide Nanocrystals: Peering into the Oleylamine–Sulfur Black Box. *J. Am. Chem. Soc.* **2011**, *133*, 5036–5041.
53. Peng, X. An Essay on Synthetic Chemistry of Colloidal Nanocrystals. *Nano Res.* **2009**, *2*, 425–447.
54. Clark, M. D.; Kumar, S. K.; Owen, J. S.; Chan, E. M. Focusing Nanocrystal Size Distributions *Via* Production Control. *Nano Lett.* **2011**, *11*, 1976–1980.
55. Qu, L.; Peng, X. Control of Photoluminescence Properties of CdSe Nanocrystals in Growth. *J. Am. Chem. Soc.* **2002**, *124*, 2049–2055.
56. Talapin, D.; Rogach, A.; Shevchenko, E.; Kornowski, A.; Haase, M.; Weller, H. Dynamic Distribution of Growth Rates within the Ensembles of Colloidal II-VI and III-V Semiconductor Nanocrystals as a Factor Governing Their Photoluminescence Efficiency. *J. Am. Chem. Soc.* **2002**, *124*, 5782–5790.
57. Donega, C.; Hickey, S.; Wuister, S.; Vanmaekelbergh, D.; Meijerink, A. Single-Step Synthesis to Control the Photoluminescence Quantum Yield and Size Dispersion of CdSe Nanocrystals. *J. Phys. Chem. B* **2003**, *107*, 489–496.
58. Joo, J.; Na, H.; Yu, T.; Yu, J.; Kim, Y.; Wu, F.; Zhang, J.; Hyeon, T. Generalized and Facile Synthesis of Semiconducting Metal Sulfide Nanocrystals. *J. Am. Chem. Soc.* **2003**, *125*, 11100–11105.
59. Stokes, A. R.; Wilson, A. A Method of Calculating the Integral Breadths of Debye-Scherrer Lines. *Proc. Cambridge Philos. Soc.* **1942**, *38*, 313–322.